Martensitic fcc-hcp transformation pathway in solid krypton and xenon and its effect on their equations of state

A. D. Rosa,[1,*] A. Dewaele,[2,3] G. Garbarino,[1] V. Svitlyk,[1] G. Morard,[4] F. De Angelis,[5] M. Krstulović,[6] R. Briggs,[7] T. Irifune,[8] O. Mathon,[1] and M. A. Bouhifd[9]

[1]*European Synchrotron Radiation Facility (ESRF), 71, Avenue des Martyrs, Grenoble, France*
[2]*CEA, DAM, DIF, 91297 Arpajon Cedex, France*
[3]*Université Paris-Saclay, CEA, Laboratoire Matière en Conditions Extrêmes, 91680 Bruyères-le-Châtel, France*
[4]*Université Grenoble Alpes, Université Savoie Mont Blanc, CNRS, IRD, IFSTTAR, ISTerre, 38000 Grenoble, France*
[5]*Dipartimento di Fisica, Universita' di Roma La Sapienza - Piazzale Aldo Moro 5, 00185 Roma, Italy*
[6]*University of Potsdam, Institute of Geosciences, Karl-Liebknecht-Str. 24–25, 14476 Potsdam-Golm, Germany*
[7]*Lawrence Livermore National Laboratory, Livermore, California 94500, USA*
[8]*Geodynamics Research Center, Ehime University, 2–5 Bunkyo-cho, Matsuyama 790–8577, Japan*
[9]*Laboratoire Magmas et Volcans, Université Clermont Auvergne, CNRS, IRD, OPGC, F-63000 Clermont-Ferrand, France*

(Received 20 December 2021; revised 8 March 2022; accepted 17 March 2022; published 15 April 2022)

The martensitic transformation is a fundamental physical phenomenon at the origin of important industrial applications. However, the underlying microscopic mechanism, which is of critical importance to explain the outstanding mechanical properties of martensitic materials, is still not fully understood. This is because for most martensitic materials the transformation is a fast process that makes *in situ* studies extremely challenging. Noble solids krypton and xenon undergo a progressive pressure-induced face-centered cubic (fcc) to hexagonal close-packed (hcp) martensitic transition with a very wide coexistence domain. Here, we took advantage of this unique feature to study the detailed transformation progress at the atomic level by employing *in situ* x-ray diffraction and absorption spectroscopy. We evidenced a four-stage pathway and suggest that the lattice mismatch between the fcc and hcp forms plays a key role in the generation of strain. We also determined precisely the effect of the transformation on the compression behavior of these materials.

DOI: 10.1103/PhysRevB.105.144103

I. INTRODUCTION

Martensitic phase transitions are fundamental first-order transformations that are, for instance, at the origin of steel hardening and shape memory effects (see Ref. [1] for review). They are diffusionless and proceed through the collective displacement of neighboring atoms. These subtle local atomic movements are at the origin of drastic changes in the materials' mechanical [2–4], transport [5], and electromagnetic [6] properties. Such transformations have been described in various materials such as pure metals and binary alloys [1,7–20], semiconductors [21], Zr-based ceramics [22], and proteins [23] that are important for the high-tech industry, planetary and life sciences. In the past decades, significant research efforts have been invested to explore the microscopic origin of martensitic transformations, but the exact transformation pathway and microstructural evolution is still debated. This lies in the very rapid nature of the first-order transformation that makes the monitoring of the phase transformation progress and mechanism extremely challenging. For this reason, most of the experimental investigations of the microstructural evolution of martensitic materials were conducted *ex situ* using a variety of techniques such as optical microscopy, scanning electron microscopy, transmission electron microscopy (TEM), and x-ray diffraction [18–20], performed on (partially) transformed systems. However, a major obstacle lies in the capacity of such techniques to disentangle the different effects occurring during the fast phase transition when it proceeds. In particular, they do not give access to the variation of the atomic distances of the parent and martensitic phase during the transformation at the relevant conditions that may play a key role in the building up and accumulation of strain in the material structure. Few *in situ* studies have been performed including neutron and x-ray diffraction or TEM [24–27] but would require higher time resolution to capture the different steps of the transformation. Only few recent studies reported the potential of proxy systems such as colloidal crystals to reveal kinetic features of martensitic transformations [28].

The heavy noble gas solids xenon (Xe) and krypton (Kr) undergo a pressure-induced phase transition, from a face-centered cubic (fcc) to a hexagonal close-packed (hcp) structure [29–32]. This transition exhibits fundamental similarities with the general features of martensitic fcc-hcp or hcp-fcc transformations observed in metals and their alloys [7,9–16] that were first described by Burgers for Zr [7]. These studies also evidenced the existence of a wide coexistence domain between an fcc and an hcp structure. In xenon, it was shown that the completion of the transformation occurs at

*angelika.rosa@esrf.fr

TABLE I. List of the experimental conditions. BL: beamline, SC: single crystal, NPD: nanopolycrystalline diamond. Raw data are presented in Figs. S1–3.

Element	Run number	BL	Technique	Beam size	Beam energy	Pressure range (GPa)	Pressure standard	Diamond type
				(μm^2)	(keV)			
Xenon	1	ID27	XRD	3×3	33.17	0–86	Au, Ni, ruby	SC
	2							
	3	BM23	EXAFS	5×5	34.56	0–155	ruby, Re	NPD
Krypton	4	ID24	EXAFS	10×10	14.33	15–68	ruby	NPD
	5							

65 GPa and the extent of the coexistence domain is not affected by temperature annealing [30,31]. As recently reported in Ref. [32], a similar behavior was observed in solid krypton but with a much wider coexistence domain of ∼400 GPa. Here again, the transition is not affected by temperature annealing attesting that it is not kinetically hindered [32]. The existence of such a large coexistence domain has been associated with the proximity of the Gibbs free energies of the fcc and hcp forms [29,33,34], which is another fundamental feature of martensitic transformations. The progressive pressure-induced fcc-hcp transition in solid heavy noble gases could represent a model system to interpret such transitions in more complex materials at the microscopic level.

The main objective of this experimental study is to exploit the progressive nature of the fcc to hcp conversion in solid Xe and Kr to *in situ* capture and characterize the different stages of the martensitic transformation. To this aim, we combined two complementary *in situ* probe techniques: x-ray diffraction (XRD) and x-ray absorption spectroscopy (XAS) that provide insights into the atomic arrangement at the bulk and local scales, respectively. We also aimed at determining the effect of this transformation on the mechanical properties of the pure and mixed fcc-hcp phases for xenon and krypton.

II. METHODS

All the experimental work was carried out at the x-ray absorption and x-ray diffraction beamlines ID24, BM23 and ID27 at the European Synchrotron Radiation Facility (ESRF) [35–37]. These three beamlines are optimal for performing very high-pressure experiments as they provide very intense, highly focused, high-energy x-ray beams. A list of the experimental conditions is presented in Table I of the main text.

A. XRD data acquisition and analysis

At the beamline ID27, monochromatic x rays with wavelength $\lambda = 0.3738$ Å were selected using a silicon (111) channel-cut monochromator and focused down to 3×3-μm^2 full width at half maximum (FWHM) using a pair of Kirkpatrick-Baez (KB) mirrors [37]. The x-ray diffraction data were collected on an MAR165 planar charge-coupled device (CCD) detector. A high-purity cerium oxide powder was used as standard to accurately determine the integration parameters (detector tilt angles, sample to detector distance, detector beam center, and instrumental peak broadening). Two kinds of diffraction images were acquired including continuous oscillation images over omega (Ω) range of ±30 ° and step-oscillations images over the same Ω range using an Ω step size of 1°. The software CRYSALISPRO was used to analyze the step-scan oscillation images [38] for the low-pressure points. The software FIT2D [39] was used to generate slices of one-dimensional diffraction patterns along the azimuth for further Rietveld refinement of textured samples (2θ range up to 17 °). The software MAUD [40] was employed to extract the unit-cell volumes, volume fractions, and coherently diffracting domain sizes (Fig. S1 of the Supplemental Material [41]).

Two independent XRD runs referred to as run 1 and run 2 were carried out at the beamline ID27 (Table I). High-purity xenon (99.999%) from the company Messer France was loaded in membrane diamond-anvil cells (DACs) equipped with single-crystal diamonds of 150- and 300-μm culet size, respectively. A hole was drilled by laser machining on preindented rhenium gasket to serve as a pressure chamber. Prior to the xenon gas loading a ruby sphere (∼3 μm in diameter), a 5-μm-thick nickel foil, and compressed gold powder pellet were placed in the pressure cavity. No additional pressure-transmitting medium such as He or Ne gas was added to the sample to avoid forming noble gas mixtures [42]. The pressure was measured using the standard ruby luminescence technique using the calibration of Dewaele *et al.* [43] and cross-checked using the unit-cell volume variation of nickel and gold using their well-established equation of states [43]. Nickel was only used as pressure calibrant at room temperature and prior to any laser annealing as it was shown that, in presence of noble gases, its compressional behavior is substantially affected by high-temperature treatment as noble gases can get incorporated in transition metals [32,44,45]. This material was also employed as yttrium aluminum garnet laser radiation absorber to evaluate the effect temperature annealing on the fcc-hcp transition in xenon. The annealing temperature was measured by analyzing the thermal emission as described in Ref. [46]. Deviatoric or nonhydrostatic stresses in the sample chamber were monitored using the analysis of the XRD peak positions of gold following well-established protocols [47]. For clarity, considering the large amount of collected XRD data points (>100), we have reported the

pressure-volume (P-V) data in Table SI of the Supplemental Material.

B. XAS data acquisition and analysis

The evolution of the local atomic arrangements of xenon and krypton with pressure was investigated at the two x-ray absorption beamlines BM23 and ID24, respectively. BM23 is the only ESRF beamline that enables micro-XAS acquisitions at x-ray energies higher than 20 keV [36]. This instrument is well suited for XAS studies in a DAC at the high-energy K edge of xenon (34.561 keV). It is equipped with a high-resolution Si(311) double-crystal monochromator and a Pt-coated KB-mirror system for x-ray beam focusing down to $5 \times 5\,\mu\text{m}^2$ (FWHM) and higher harmonics rejection. Two ion chambers were used to measure the incident (I_0) and transmitted (I_t) intensities filled with appropriate gas mixtures of krypton and helium to achieve signal absorption of 30 and 70%, respectively. The local structure of krypton (K-edge energy of 14.385 keV) was investigated at the energy-dispersive XAS beamline ID24 [35]. At this instrument, a high-intensity and highly focused x-ray beam of $10 \times 10\,\mu\text{m}^2$ (FWHM) is generated by a Si(111) polychromator and rhodium-coated mirrors. The incident and transmitted intensities were recorded using a FReLoN CCD camera as described in Rosa *et al.* [32].

Three independent XAS runs referred to as run 3, run 4, and run 5 were performed (Table I). Run 3 was devoted to xenon and performed at BM23 while runs 4 and 5 were focused on krypton and carried out at ID24 (examples of raw data are presented in Fig. S2 and Fig. S3 of the Supplemental Material). Typical data acquisition times were 30 min and 50 ms at BM23 and ID24, respectively. For these runs all the DACs were equipped with nanopolycrystalline diamonds that enable acquiring glitch-free, high-quality extended x-ray absorption fine structure (EXAFS) data [48]. As for the experiments at ID27, a laser-drilled hole on a preindented rhenium gasket was employed as pressure chamber. The high-purity noble gases were loaded together with a small ruby sphere used for pressure measurements following a similar procedure as described above. In run 3, at pressures higher than 90 GPa, the pressure was determined by XRD using the unit-cell volume variation of the rhenium gasket [49]. Diffraction data were collected at two distinct positions in the DAC to evaluate the pressure gradient across the sample. For these measurements, an MAR165 diffraction detector was installed at BM23 at a distance of 197.37 mm from the sample and XRD images were acquired without oscillation at a wavelength of 0.3594 Å (34.5 keV). The dimensions of the diamond culets and the investigated pressure domains for the different runs are listed in Table I.

For both xenon and krypton, we used a similar data reduction procedure to determine the local lattice distortion in the first stacking layer and, to follow qualitatively the evolution of potential lattice distortions up to the third stacking layer (Fig. 1). EXAFS spectra were normalized, converted from energy to k space $\chi(k)$, and Fourier transformed using a Kaiser-Bessel envelope and further analyzed without phase shift using the ARTHEMIS software package [50].

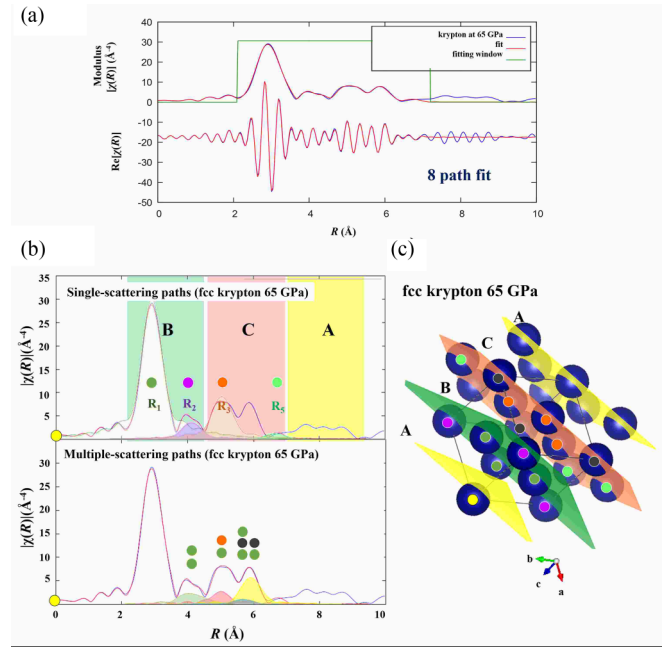

FIG. 1. (a) Top panel: Modulus of the krypton K-edge EXAFS function collected at 65 GPa representing the distribution of average interatomic distances (R) seen from a central absorbing atom. The modulus is obtained by Fourier transform of the normalized K-edge EXAFS functions (Figs. S2 and S3, Supplemental Material) after their conversion from energy to k space and multiplication by k^2 ($k^3[\chi(k)]$). The amplitude of different peaks is proportional to the scattering probability. The blue lines represent the modulus (top) and the real part (bottom) of the original data; the green line represents the fitting window for the EXAFS analysis (phase shifted). The red lines represent the adjusted EXAFS spectrum. (b) Bottom panel: Modulus of the EXAFS function as above (blue line) plotted together with the moduli of the four most probable single-scattering paths (top) and the four most probable multiple-scattering paths (bottom) adjusted in the fit. (c) For clarity, a section of an fcc structure with the stacking sequence *ABCA* is shown on the right. Atoms involved in the scattering paths emerging from the central atom (marked with a yellow circle) are highlighted with circles of different color, corresponding to symbols and interatomic distances as marked in the EXAFS modulus plots in (b) on the left.

EXAFS is sensitive to local distortions including coexisting domains, stacking faults, and grain boundaries, which cannot be easily quantified by XRD. The focus of the present EXAFS analysis resided on the identification of the extent of such local structural distortions in the bulk sample. We aimed at monitoring the growth of hcp stacking faults having smaller lattice volumes than the host fcc phase as seen using XRD in Kr by Rosa *et al.* [32].

The signal obtained in transmission XAS geometry represents the average of atomic environments probed around an absorbing atom. Therefore, the signal contains contributions from atoms in fcc and hcp structural environments. The signal contribution of each phase is linearly dependent on its volumetric fraction in the present case. The most intense signals of both forms, fcc and hcp, emerge from scattering of the first and second stacking layers (Fig. 1). In these environments, an atom exhibits an equivalent number of next-nearest neighbors

(N_1 and N_2) and also similar interatomic distances (R_1 and R_2) if the two forms have the same unit-cell volumes. Beyond the third stacking layer the scattering signals are different in the two phases, that exhibit either an *ABCABC* stacking sequence (fcc) or an *ABABAB* stacking sequence (hcp) (Fig. 1, R3 and R5). Because of the similarities of the scattering signals for the hcp and fcc phases in the most intense part of the signal and the expected low lattice volume difference of only 4% between fcc and hcp forms [32], we did not intend to extract individual lattice volumes and volumetric fractions for the coexisting phases from the EXAFS data. The contributions of the coexisting forms could only be resolved at higher signal frequencies that exhibit low amplitudes (Fig. 1). The refinement of the volume fractions for the two coexisting structures would have therefore increased the number of fitted variables beyond the number of independent points.

The present EXAFS analysis mainly aimed at extracting the average atomic distances for the next-nearest neighbor R_1 which emerges from the scattering contribution of the coexisting fcc and hcp forms, and the variation of R_1 (σ_1) across the compressional anomaly. The volumetric growth of dense hcp stacking faults would reduce the average next-nearest neighbor distances R_1 seen from XAS compared to the equilibrium distance R_0 observed for the bulk parent fcc phase using XRD. In previous studies the observed differences between R_1 and R_0 values from XAS and XRD were assigned to the presence of significant atomic vibrational anisotropies that result systematically in higher R_1 values compared to R_0 (e.g., Ref. [51]). This work is focused on the relative and not the absolute pressure-induced changes of interatomic distances near the observed compression anomaly to test the hypothesis if dense hcp stacking faults form in this pressure interval.

In the present EXAFS analysis, all fittings were performed using a single structural input model (fcc or hcp). To verify the robustness and independence of results for the first two scattering paths, two adjustments were carried out for several EXAFS spectra, with the fcc and hcp models, respectively. For each EXAFS fitting, the structural input models were calculated using the equation of states of fcc and hcp Kr and Xe obtained from XRD. Theoretical backscattering amplitudes and phase-shift functions for fcc and hcp phases were computed subsequently using the FEFF *ab initio* code included in ARTHEMIS. The adjustments included a minimum of two and up to eight scattering paths similar to those employed by Filipponi and DiCicco [52]. The eight scattering paths included four single-scattering paths up to the fifth shell excluding the direct fourth-shell scattering path due to its low probability (Fig. 1); four multiple-scattering paths that have an important contribution to the EXAFS function such as the acute triangle in the first shell, the obtuse triangle including atoms in the third shell; one forward- and one double-forward scattering path to atoms of the fourth shell. For each scattering path the interatomic distance (R_i) and its distribution ($\sigma^2{}_i$) were adjusted.

For xenon, we obtained lower EXAFS data quality at pressures below 10 GPa. In this case, the adjustment window was shorter than the one employed for spectra obtained at higher pressure. The Xe EXAFS functions were adjusted in the k range between 3 and 9 $Å^{-1}$ (fitting window set between 2 and 5.7 Å) at pressures below 10 GPa and up to 14 $Å^{-1}$ (fitting window set between 2 and 8.5 Å) beyond this pressure. Xe EXAFS data taken at the lowest pressure (5.9 and 8.5 GPa) were fitted using an fcc structural model that contained 20 independent points and 15 adjusted parameters including 7 structural parameters from 2 paths (R_1 and R_2) with each individually fitted parameters R and σ^2, the energy shift ΔE, and 8 background parameters. At higher pressures between 15 and 53.1 GPa, in the coexistence domain of the fcc and hcp forms, the Xe EXAFS fittings were performed either with the fcc or hcp structural input model. Above 53.1 GPa and up to 158 GPa, only the hcp structural input model was used. Both adjustments using the fcc or hcp structural model contained up to 60 independent points and 33 adjusted parameters including 17 structural parameters from 8 paths with each individually fitted parameters R and σ^2, the energy shift ΔE, and 16 fitted background parameters.

All Kr EXAFS functions were fitted using the fcc structural input model due to the low volume fraction of the hcp phase (<20%) in the investigated pressure range. The fitted k range was set from 3 to 10.5 $Å^{-1}$ (fitting window from 2 to 8 Å). All fits were performed with k weighting of 1, 2, and 3 and background adjustments to diminish correlations between σ^2, R, and ΔE_0.

The results are listed in Table SII and Table SIII. The relative uncertainty on the first-neighbor distances (R_1) is smaller than (5×10^{-3}) over the entire pressure range. The error on the extracted bond distance variation is on the order of 3%. Variations of ΔE may arise from the growing hcp phase that modifies the white line as shown in Ref. [32] for krypton. The R factor is listed for each fit and presents a measure of the misfit between the raw data and the adjusted spectrum in % (an R factor of 0.02 indicates a 2% misfit to raw data).

III. RESULTS AND DISCUSSION

A. X-ray diffraction study of xenon

As presented in Table I, two independent XRD runs were carried out on solid xenon. Following the same methodology as for krypton [32], run 1 was devoted to the detailed investigation of the fcc to hcp martensitic transformation, the effect of temperature annealing, and the determination of the equation of state (EoS) of fcc and hcp xenon, in a wide pressure regime up to 85 GPa. A large number of data points (75 data points) were collected in this run to increase the precision on the determination of the EoS parameters. As it was conducted in a large overlapping pressure interval (∼40 GPa) with run 1, run 2 was used to control the consistency of the obtained results, increase their precision and robustness, and further study the effect of temperature annealing on the fcc-hcp transition.

A series of diffraction images from run 1, recorded between 1 and 73.7 GPa, is presented in Fig. 2. At 1.09 GPa, an fcc single crystal is observed. At this pressure, the intensity distribution in the (111) Bragg reflection is homogeneous and no trace of diffuse scattering is observed. At slightly higher pressure ($\Delta P \sim 0.3$ GPa), this diffraction peak largely deforms and a weak diffuse intensity is growing up in its vicinity. A careful analysis of the pressure-induced intensity

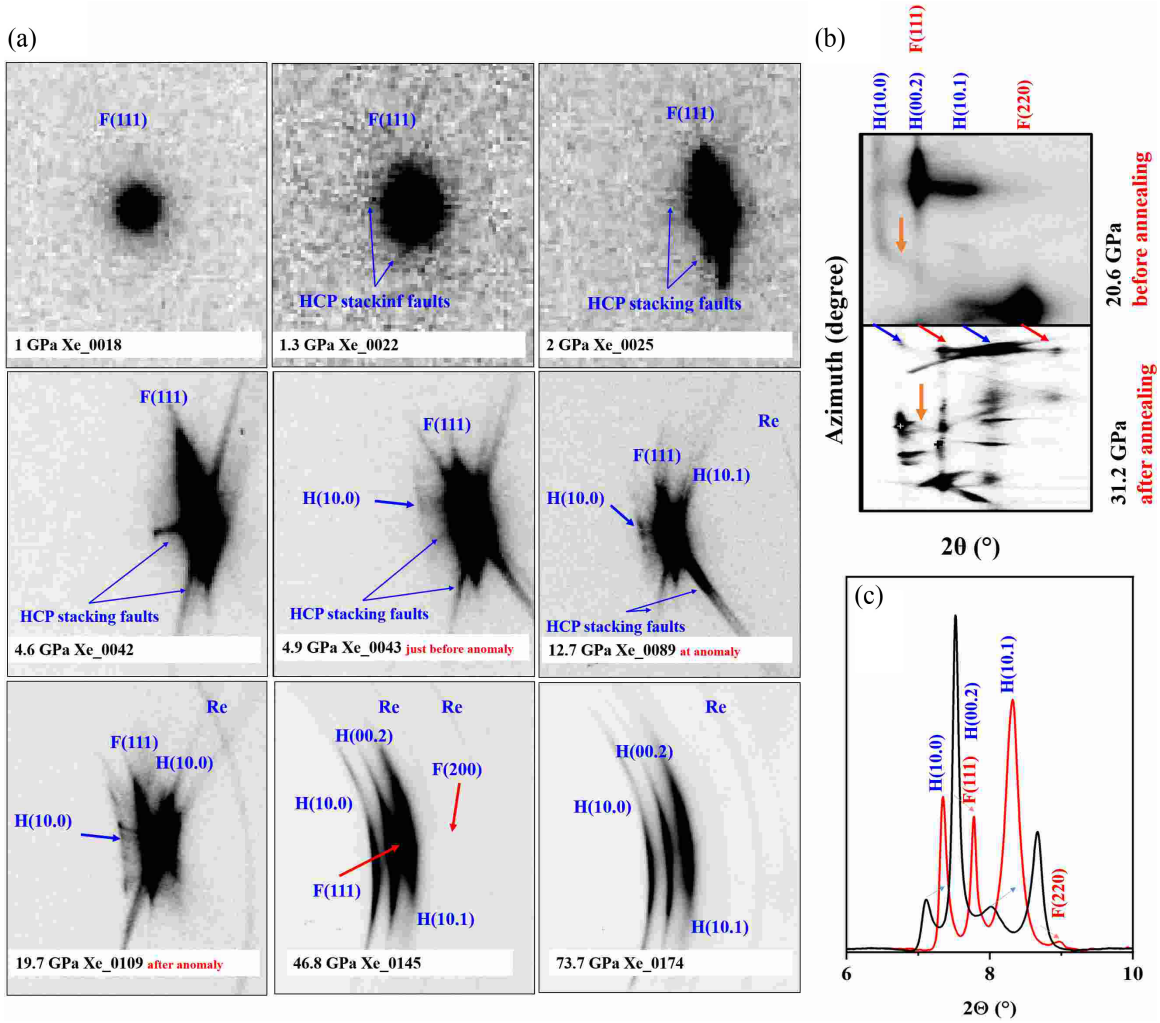

FIG. 2. (a) Left panels: Series of diffraction images from run 1 on pure xenon, showing the evolution of the xenon fcc (111) reflection [denoted as F(111)] with increasing pressure, the onset of the x-ray diffuse scattering linked to the emergence of the hcp phase and hcp Bragg reflections [denoted as H(10.0), H(00.2), and H(10.1)] after completion of the phase transition at ∼74 GPa. (b), (c) Right panels: X-ray diffraction images (top) and corresponding integrated patterns (down) from run 2 on xenon before and after annealing at $T = 2400$ K. Note the pressure increase due to temperature annealing.

transfer from the fcc to the hcp phase along the [111] direction indicates that the appearance of x-ray diffuse signal is linked to the onset of the fcc/hcp martensitic transition. The presence of x-ray diffuse scattering was reported previously for xenon and krypton [30–32] and related to the presence of an increasing number of stacking faults (SFs) along the fcc [111] direction. For xenon, the onset of the fcc/hcp transition is precisely located at 4.9 GPa. As shown in Fig. 2, above this pressure a progressive splitting of the (111) fcc reflection into the hcp (100), (002), and (101) reflections is recorded on panoramic XRD images. Single-crystal XRD measurements at this pressure confirmed that the martensitic phase transition in xenon produces an hcp phase with the expected orientation relation: fcc (111)//hcp (0001) and fcc [1–11]//hcp [1-210].

Similarly to krypton [32] and as shown in Fig. 2(b), the x-ray diffuse signal present at ambient temperature remains very intense after temperature annealing ($T > 2400$ K) in the entire pressure domain of fcc-hcp phase coexistence. This strongly suggests that the fcc-hcp transition and the presence of hcp SFs are not due to nonhomogeneous stress distribution in the pressure cavity. This is also supported by the deviatoric stress analysis of the XRD peak positions of the gold sample in run 1 and run 2 (Figs. S4 and S5, Supplemental Material). This analysis reveals quasihydrostatic pressure conditions in the sample chamber up to ∼15 GPa in run 1 and over the entire investigated pressure range in run 2. At pressures above ∼15 GPa, a small deviatoric stress of 0.14 GPa develops in run 1 that increases to a moderate value of 0.5 GPa at 71 GPa. For comparison, this value is on the same order as in helium, a quasihydrostatic pressure medium [47], although an increase in strength with rare-gas weight is expected. Martensitic transitions commonly induce shape changes of a transforming crystal during the collective shuffling of atoms [1]. This shape change can lead to the buildup of internal stress in the crystal that is known as transformational stress [1]. The formation of multiple equivalent-sized martensite variants can counterbalance the shape change and limits thus the transformational stress [1,53]. The same mechanism could also release non-

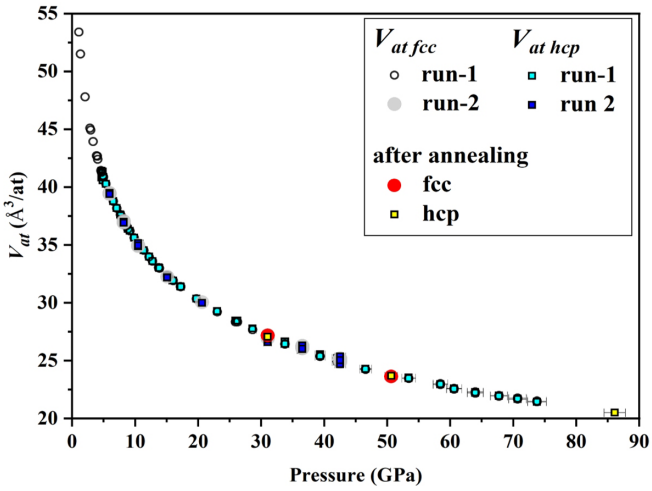

FIG. 3. Pressure evolution of the atomic volume V_{at} (Å^3) for the fcc and hcp phases of xenon. The pressure has been determined using the ruby luminescence technique (Dewaele *et al.* [43]) up to 60 GPa. Beyond this pressure the pressure from the unit-cell volume of gold was used and the EoS reported in Dewaele *et al.* [43]. Uncertainties on V_{at} are on the order of 10^{-3} and smaller than the symbol size. The symbols for the fcc phase of run 2 and after annealing have been enlarged for better visualization but bear the same uncertainties as other points. Note that the effect of temperature annealing on V_{at} is negligible and that there is little difference between V_{at}/fcc and V_{at}/hcp that is below 1% (Table SI). The literature data are presented in the left inset panel.

hydrostatic stress that is usually built in the diamond-anvil cell by thinning of the gasket. The very low deviatoric stress observed in gold above the transition pressure (Figs. S4 and S5) suggests that this mechanism could be at work here.

B. Anomalous compression behavior

From run 1 and run 2, we have accurately determined the effect of the martensitic transformation on the equation of states of fcc and hcp xenon. In particular, we examined the effect of the increasing concentration of stacking faults on these EoS. We have finely explored the low-pressure regime to better constrain the ambient pressure atomic volume (V_0) and examined the effect of temperature annealing. The pressure variation of the atomic volume of fcc and hcp xenon from this study are presented in Fig. 3 and compared to the literature [30,54,55] in Fig. S6 (Supplemental Material). The *P-V* data from runs 1 and 2 are in excellent agreement in their overlapping pressure domain for both the fcc and hcp forms. As evidenced in Fig. 3 and S6 (Supplemental Material), the present dataset exhibits lower dispersion than the literature ones, resulting in a more accurate determination of the equation of state parameters. From the absence of observable deviation of the atomic volume of xenon after high-temperature treatment, we also could confirm that, similarly to krypton [31,32], temperature annealing has a negligible effect on the compression behavior of xenon.

The equation of state parameters, i.e., the unit-cell volume at ambient pressure V_0, bulk modulus K_0, and first derivative K' for fcc and hcp xenon were derived by adjusting the *P-V* data to a Vinet EoS using the software EOSFIT [56], taking into account the uncertainties on P and V. The obtained V_0, K_0, and K' for fcc and hcp xenon are listed together with literature values in Tables II and III, respectively.

They are in good agreement with the values of Dewaele *et al.* [57] but substantially deviate from the ones reported in Refs. [30,31]. This could originate from the high number of measured data points (75) in the present work, in particular at low pressure, where a slightly larger data dispersion can induce a large error in V_0. As for krypton [32], a near-ideal c/a ratio for hcp structures [$\sqrt{(8/3)} = 1.633$] is observed for all the hcp data points (Table I and Fig. S7 top panel, Supplemental Material), attesting to a similar reduction of the two crystallographic axes a and c of xenon with increasing pressure. The axial ratios of most hcp metals fall in the range $1.57 < c/a > 1.65$ and show very little variations with pressure as discussed in Kenichi [58]. The near to ideal c/a ratio found for Xe over the probed pressure range of 1.631(2) may rule out the existence of an intermediate orthorhombic close-packed structure as previously proposed [29,59] and may rather indicate a progressive martensitic transformation related to the increasing fraction and thickening of stacking faults in the material. In krypton, Rosa *et al.* [32] observed a slight deviation from the near-ideal c/a ratio especially in the low-pressure regime for which the hcp volume fraction remains below 20% (Fig. S7 bottom panel, Supplemental Material). This may suggest a structural distortion of the hcp SFs seeds from the ideal hcp structure.

Another source of uncertainty in the determination of the EoS parameters of xenon could arise from the nature of the fcc/hcp martensitic transformation. Indeed, it was shown that krypton exhibits an anomalous compression behavior related to the presence of an increasing number of hcp domains of nanometric size [32]. This singular behavior was determined from the correlation between the pressure dependence of the volume fraction of the hcp phase and the anomaly in the normalized pressure, F, versus Eulerian strain, f [60,61], where $f = [(V/V_0)^{-2/3} - 1]/2$ and $F = P/[3f(1+2f)^{5/2}]$. The Ff plot analysis is a standard method to detect compression anomalies that are not obvious in the regular evolution of the compression curve (*P-V* plot). We have conducted a similar Ff plot analysis for xenon. As shown in Fig. 4(a), a clear deviation to a linear variation is evidenced in fcc xenon at a pressure of ~15 GPa. As already mentioned, such a nonlinear effect has also been determined in solid krypton at slightly higher pressure (~20 GPa) [32], suggesting a systematic evolution of the underlying microscopic mechanism during the fcc/hcp martensitic transition in heavy noble solids [Fig. 4(b)].

To correlate the observed Ff plot anomaly with the hcp volume fraction (VF_{hcp}), we have determined its evolution with pressure using multiphase Rietveld refinement of the XRD patterns using the intensity ratio of all Bragg reflections. As presented in Fig. 5, we found a progressive pressure variation of VF_{hcp} reaching ~100% at ~80 GPa. This behavior is contrasting with the one reported by Cynn *et al.* [30] and Errandonea *et al.* [31], which exhibit a much sharper transformation. This may be related to the differences in the analysis techniques, i.e., Rietveld refinement (this study) versus manual relative peak height analysis (previous works). It is worth

TABLE II. Equation of state for fcc xenon: model and fit parameters V_0, K_0, K', pressure range, and number of data points from this work and the literature.

fcc xenon	Model	V_0 (Å^3)	K_0 (GPa)	K'	P range (GPa)
This study	Vinet	235.15(9)	4.54(2)	6.26(1)	1–74 (75 points)
Dewaele *et al.*, 2012 [57]	R.-Vinet[a] (0 K)	233.76	4.887	6.18(5)	4–50 (20 points)
Errandonea *et al.*, 2002 [31]	BM[b] third	249.75	4.3(6)	5.7(5)	1.5–41 (8 points)
Cynn *et al.*, 2001 [30]	BM[b] third	252.21	3.6(5)	5.5(4)	3–50 (29 points)

[a]R.-Vinet: Rose-Vinet.
[b]BM: Birch-Murnaghan.

noting that the complete fcc/hcp conversion in xenon occurs at much lower pressure than in krypton for which the pure hcp phase is expected at ∼400 GPa. At 15 GPa, the pressure at which the anomaly in the Ff plot is observed, VF_{hcp} reaches ∼40%, a value that is twice as large as for krypton (VF_{hcp} at anomaly ∼20%). It is also worth noting that the volume fraction VF_{hcp} is not significantly affected by temperature annealing.

As presented in Fig. 6, we have also determined the pressure evolution of the coherently diffracting domain size for fcc (CDS_{fcc}) and hcp (CDS_{hcp}) xenon. These quantities were obtained by adjusting the XRD Bragg reflection profiles using Popa's analytical approximation implemented in the software MAUD [62]. We observe a strong reduction with pressure of CDS_{fcc} while the CDS_{hcp} is not significantly affected. This behavior is similar to the one previously observed for krypton [32]. This suggests a generic transformation mechanism in krypton and xenon at the first stages: The increasing fraction of nanometric hcp SFs propagates, breaks fcc domains into smaller ones, and interconnects gradually through the material at a regular pressure rate. The data suggest that the interconnection of hcp domains starting from ∼5 GPa leads to the gradual deviation from a regular compression behavior in fcc xenon (Fig. 4). It is worth noting that this pressure coincides with the appearance of the first hcp diffraction peaks (Fig. 2). At pressures higher than 15 GPa beyond the inflexion point of the compression anomaly, the CDS of the fcc phase does not reduce further contrary to its volume fraction, while the CDS of the hcp phase increases slightly. These observations are similar to those made on krypton (inset panel of Fig. 6). This suggests that beyond the compression anomaly a modification in the fcc-hcp transformation mechanism occurs that balances the effect of transformational and compressional stresses.

C. XAS study of krypton and xenon

In addition to XRD, we have carried out extended x-ray absorption fine structure experiments to follow the pressure evolution of the local atomic arrangement of krypton and xenon during the martensitic transformation. EXAFS provides accurate structural data of the average local atomic environment that complement the information on the individual phases obtained by XRD. In the present study, high-quality EXAFS data of krypton and xenon were acquired in a diamond-anvil cell (Figs. S2 and S3, Supplemental Material). For both xenon and krypton, we used the same data analysis procedure to investigate next-nearest interatomic distances R_i between a central absorbing atom and neighboring atoms and their distributions ${\sigma^2}_i$.

Three EXAFS runs were performed (Table I). In run 3, we have collected EXAFS data of xenon in an extended pressure domain up to 155 GPa to monitor the structural deviations from the ideal fcc and hcp configurations during and after completion of the martensitic transformation. More data points were collected in runs 4 and 5 on krypton to investigate with a higher resolution the martensitic transition in the vicinity of the compression anomaly (Table I). These data were also used to compare the interatomic potential forces to previously reported ones obtained using Monte Carlo simulations [63].

TABLE III. Equation of state for hcp xenon: model and fit parameters V_0, K_0, K', the pressure range, number of data points from this work and the literature.

hcp xenon	Model	V_0 (Å^3)	K_0 (GPa)	K'	P range (GPa)
This study	Vinet	118.71	4.24(4)	6.35(3)	4–86 (65 points)
Dewaele *et al.*, 2012 [57]	R.-Vinet[a] (0 K)	114.82	4.887 fixed	6.2955	10–260
Cynn *et al.*, 2001 [30]	BM[b] third	126.10	4.3(3)	4.9(1)	52–127 (15 points)

[a]R.-Vinet: Rose-Vinet.
[b]bBM: Birch-Murnaghan.

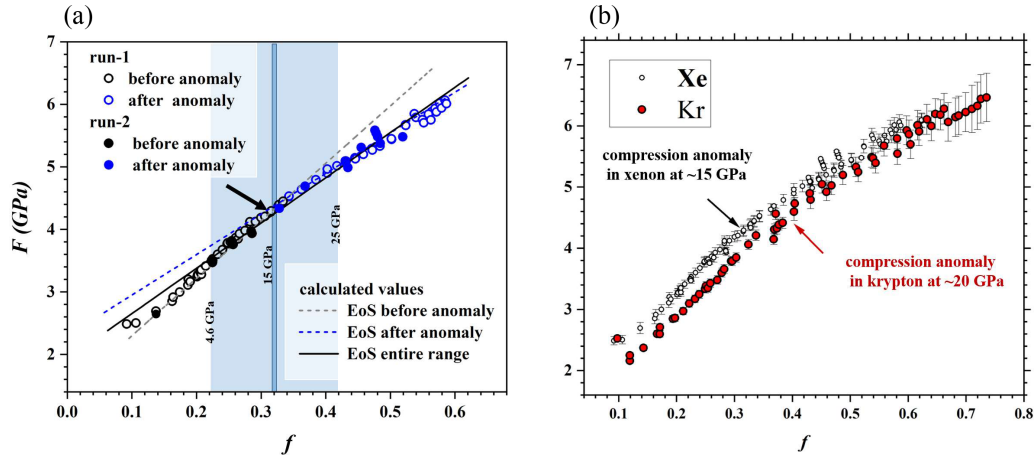

FIG. 4. (a) Normalized pressure, F in GPa, vs Eulerian strain f, for the fcc phase of xenon and (b) compared to the one found for krypton in a previous work [32]. The gray and blue dashed lines correspond to calculated values from fitted EoS using the data obtained before (open symbols) and after (filled symbols) the anomaly. The black solid line corresponds to the data fitting over the entire P domain (up to 74 GPa). Uncertainties are 2% for the pressure and are within the symbol size for the Eulerian strain f and F. The interval of the compression anomaly where a deviation from a linear compression behavior occurs is highlighted by the light-blue shaded area. The turnover over point of the compression behavior is indicated with an arrow and a dark-blue line in (a). It appears for xenon at ∼15 GPa and it is derived from the crossing of the two independent EOS fits, before and after the anomaly. Note that we observed a similar behavior in krypton [32] as shown in (b), where the turnover in compression behavior is indicated by a red arrow.

As outlined in Sec. II B, the principal objective of the present EXAFS analysis is to constrain the pressure variation of the average next-nearest neighbor distance (R_1) and its distribution ($\sigma^2{}_1$) in order to extract average local structural properties of the bulk material that contains both the fcc and hcp forms. These average properties may progressively deviate from observations of the individual structural properties of the host fcc phase obtained using XRD due to the growth of hcp SFs with reduced lattice volumes that cannot be distinguished easily using XRD.

As represented in Figs. 1, S1, and S2, long-range EXAFS data were acquired up to a k of 16 Å^{-1} providing interatomic distances and their distributions up to the third stacking layer

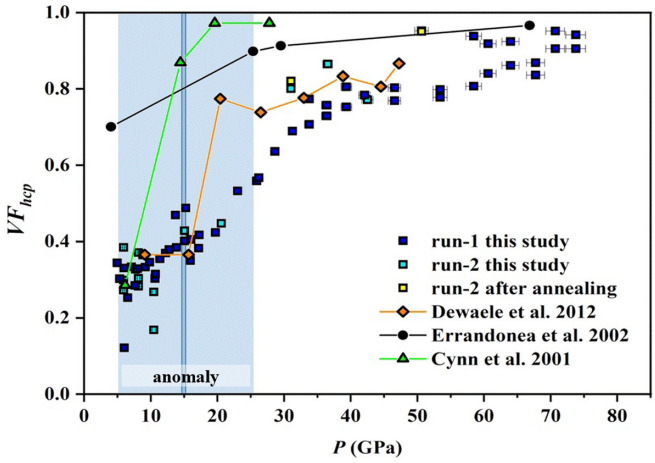

FIG. 5. Pressure evolution of the hcp xenon volume fraction (VF_{hcp}) extracted from Rietveld analysis of run 1 and run 2 (dark- and light-blue squares, respectively). Yellow filled squares indicate the data points obtained after temperature annealing in run 2. VF_{hcp} from the literature obtained by Rietveld refinement of the intensity ratios of the fcc (200) and fcc (111)+hcp (002) reflections are indicated. Blue bar: pressure at which the anomalous compression behavior is observed. At this pressure, VF_{hcp} is ∼40%. In this study, the uncertainty on VF_{hcp} is on the order of 6% and smaller than the symbol size.

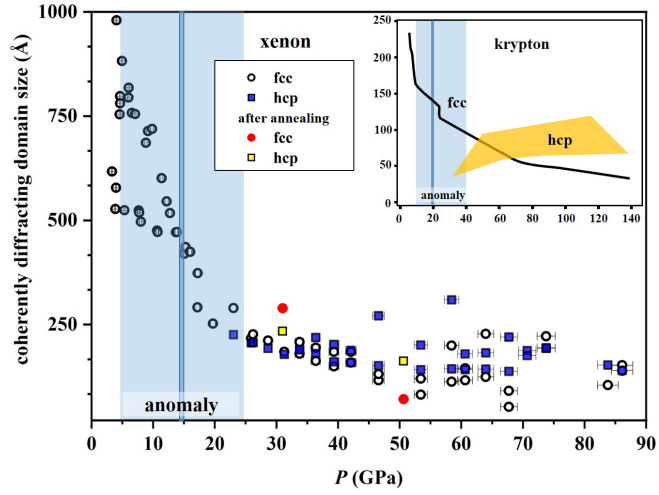

FIG. 6. Pressure dependence of the coherently diffracting domain size (*CDS*) extracted by Rietveld analysis using Popa's analytical approximation for the fcc and hcp phases of xenon: circles and blue squares. The red and yellow symbols indicate the data points obtained after temperature annealing. The uncertainties on *CDS* extracted from Rietveld are on the order of 15 Å and smaller than the symbol size. The blue area highlights the pressure domain of the compression anomaly and the blue bar its inflection point. The pressure dependence of the *CDS* for the fcc and hcp krypton as reported in Ref. [32] is schematically represented in the inset panel.

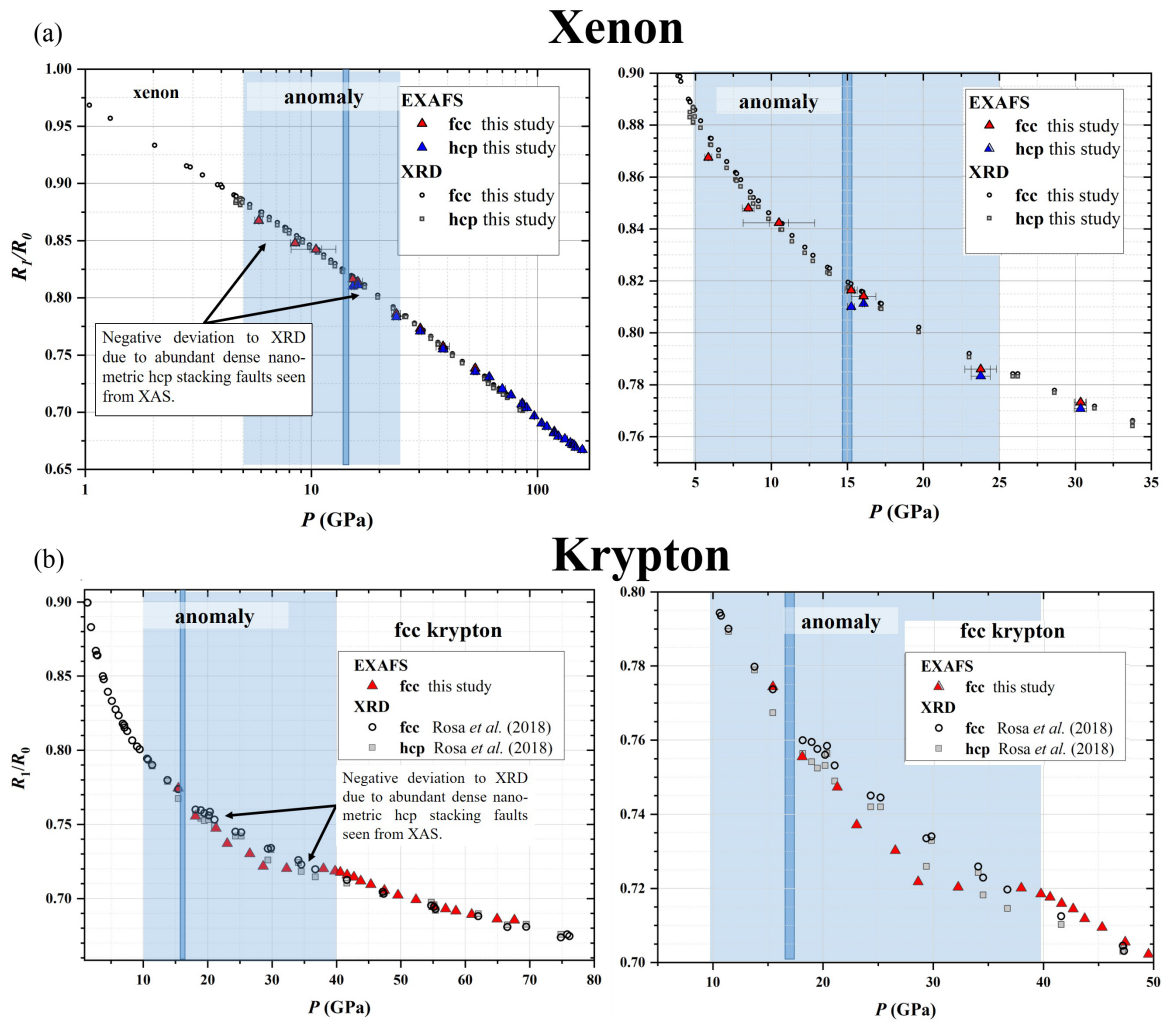

FIG. 7. (a) Pressure evolution of the first-nearest neighbor interatomic distances in fcc and hcp xenon normalized to its value at ambient pressure (R_1/R_0). Data obtained from EXAFS fitting using either the fcc or the hcp phase as input model are compared to calculated values using the EoS of fcc and hcp xenon derived from XRD in this study (Tables II and III). R_0 was calculated from V_0 as obtained from the EoS of the present XRD data. A logarithmic pressure scale for xenon data was chosen to highlight the small deviations between results of different fit models and x-ray probes at low pressures. Uncertainties are smaller or on the order of the symbol sizes. (b) Pressure evolution of the first-nearest neighbor interatomic distance of fcc krypton normalized to its value at ambient pressure (R_1/R_0). Data obtained from EXAFS analysis in this work are compared to those acquired from a previous XRD study [32]. R_0 values for fcc and hcp krypton were calculated from a previous EoS study [32]. The pressure domain of the compressional anomaly observed in this study in xenon and by Rosa *et al.* [32] in krypton are highlighted by a blue-shaded area and the inflexion point of the anomaly is indicated with a blue bar.

of the close-packed planes. Fcc and hcp structures, respectively, follow an *ABCABCABC* and *ABABABAB* pattern type (Fig. 1 for fcc). The most intense scattering signals of the fcc and hcp forms emerge from paths in the first and second stacking layer. These paths exhibit an equivalent number of next-nearest neighbors and bond distances if the two forms have the same lattice volumes. This complicates the extraction of volumetric fractions and individual lattice volumes from EXAFS fitting, which was therefore not attempted in this analysis. We used the long-range EXAFS data to determine deviations from the ideal fcc and hcp forms seen from XRD by extracting the average next-nearest bond distance (R_1) and its distribution ($\sigma^2{}_1$) seen using XAS data. The evolution of average interatomic distances up to the higher stacking layers were also determined (R_2, R_3, R_5) but are only discussed qualitatively in comparisons to R_1 as they have higher uncertainties. For clarity, the resulting pressure variations of the extracted bond distances of all scattering paths [R_1, R_2, R_3, R_5; see Fig. 1(b)] and their distributions are reported in Tables SII and SIII (Supplemental Material) for xenon and krypton, respectively.

D. Origin of the compressional anomaly

The evolution of the normalized first-nearest neighbor interatomic distance R_1/R_0 for fcc and hcp xenon obtained from the EXAFS and XRD analysis are presented in Fig. 7(a). Above ~25 GPa, the results of both x-ray approaches are in good agreement within their mutual uncertainties. Below this pressure, the average first-neighbor Xe-Xe interatomic distances extracted from the EXAFS data are slightly shorter than those obtained using XRD. However, no definitive conclusion

could be drawn from the EXAFS data on xenon regarding the microscopic origin of the compression anomaly due to the few data points sampled in the pressure interval where it occurs [Fig. 7(a)]. At pressures above 60 GPa, the first-neighbor Xe-Xe distances extracted from EXAFS are slightly larger than those measured by XRD. Such positive deviations were previously related to the existence of anisotropic vibrational modes [51].

The larger number of EXAFS data points collected on krypton in runs 4 and 5 in the vicinity of the compression anomaly enabled a more detailed interpretation of its origin. As presented in Fig. 7(b), from the EXAFS data, we observe a strong reduction of the first average neighbor distance (here referred to as Kr-Kr) between ∼18 and 36 GPa that is very difficult to assess from the XRD data [32]. We relate this observation to the formation of a large amount of dense hcp SFs in fcc Kr in the pressure interval of the compression anomaly. As it has been demonstrated in our previous XRD data [32], hcp SFs exhibit shorter next-nearest neighbor distances than the parent fcc phase. This observation is supported by the slightly smaller c/a ratio of initial hcp Kr especially in the pressure interval of the anomaly compared to the ideal value [$\sqrt{(8/3)} = 1.633$] (Fig. S7 bottom; Fig. 4 in Rosa *et al.*, [32]). Under the assumption that the interatomic distance parallel to the (111)fcc//(0001) hcp plane is unchanged (this assumption is acceptable when the transition proceeds *via* shuffling motion according to Burgers [7]), the c/a ratio directly corresponds to the (111) interplane distances. Therefore, the smaller c/a ratio of hcp Kr provides a reasonable support for the shorter interatomic distance measured in the stacking faults. It is worth noting that the inflexion point of the compression anomaly in fcc krypton observed at ∼20 GPa from XRD occurs at the onset of the negative deviation of Kr-Kr interatomic distances probed by EXAFS. At pressures below or above the compression anomaly, the average Kr-Kr interatomic distances obtained using EXAFS and XRD [for the fcc phase, Fig. 7(b)] are in good agreement. We also note that the c/a ratio extracted from XRD of hcp Kr converges at ∼100 GPa (hcp krypton volume fraction of 35%) towards a near-ideal c/a value of 1.631 [Fig. 7(b)].

A similar conclusion can be qualitatively drawn regarding the pressure evolution of the interatomic distances of the second, third, and fifth next-nearest neighboring atom extracted from EXAFS that deviates from the ideal fcc interatomic distances in the region of the compression anomaly for both Xe and Kr (Fig. S9). Interestingly, far away from the anomaly at ∼60 GPa, the interatomic distances in the second and third stacking layer (R_2, R_3, and R_5) are closer to those of the fcc phase than to those of the hcp phase obtained by XRD [Fig. S9(a)]. This suggests the presence of a large fraction of boundary defects between hcp domains that have a local atomic arrangement close to an fcc lattice. Such defects could be located on hcp twins or grain boundaries.

As shown in Fig. 8, the compression anomaly is also evidenced in the pressure variation of the first-neighbor distance distribution $\sigma^2{}_1$ in krypton and to a lesser extent in xenon. In krypton, the fitted values of $\sigma^2{}_1$ up to 25 GPa show a strong deviation from the $\sigma^2{}_1$ calculated by Aziz and Slaman (Hartree-Fock-dispersion potential model B) [64] and reported by DiCicco *et al.* [63] using a hard-sphere model for

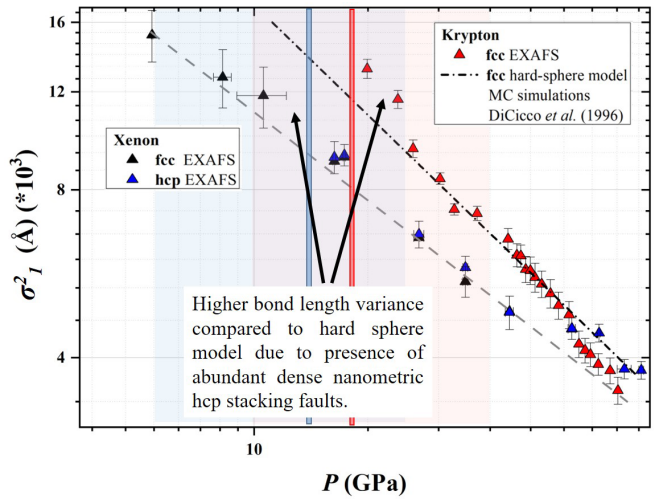

FIG. 8. Pressure variation of the fitted first-neighbor distribution of krypton and xenon ($\sigma^2{}_1$) obtained from EXAFS. The data are compared to Monte Carlo simulation results using a hard-sphere model approach [63] for fcc krypton (denoted as MC in the figure legend). A linear trend is expected for a regular compression behavior. Due to the lack of computational studies for fcc/hcp xenon, we have drawn a linear line through the data points before and after the compression anomaly as a guide for the eyes.

fcc krypton. This deviation is reduced but still persistent up to ∼40 GPa, suggesting a high degree of structural disorder for fcc krypton in the pressure interval of the compression anomaly. A similar behavior occurs for xenon and for the second, third, and fifth nearest neighbors in krypton and xenon (Fig. S10, Supplemental Material). Overall, the pressure dependence of $\sigma^2{}_1$ is consistent with the interpretation derived from the evolution of R_i: The increasing fraction of hcp SFs in the fcc structure induces a high degree of structural disorder. This effect is more pronounced in the pressure domain of the compression anomaly because the two structures have differing unit-cell volumes at these conditions. Our conclusion is strengthened by our observations beyond the compression anomaly and up to 60 GPa: In this pressure domain we observe a reduction of $\sigma^2{}_1$ to the predicted trend of the atomic interaction potential in the hard-sphere model of Aziz and Slaman [64]. Beyond 60 GPa, the bond distribution of krypton and xenon deviates from the linear variation expected for a regular compression behavior. In xenon, this behavior could be explained by the presence of a large fraction of boundary defects between hcp domains in the final sample microtexture close to the completion of the transition.

IV. MECHANISM OF THE MARTENSITIC TRANSFORMATION

The combined results of EXAFS and XRD suggest a multistage growth of hcp SFs in the heavy noble gases krypton and probably in xenon. The proposed microscopic mechanism of the martensitic transformation is presented in Fig. 9. Prior to the transformation, the starting material is a high-quality single crystal with well-defined Bragg reflections and without detectable x-ray diffuse scattering that would be the signature

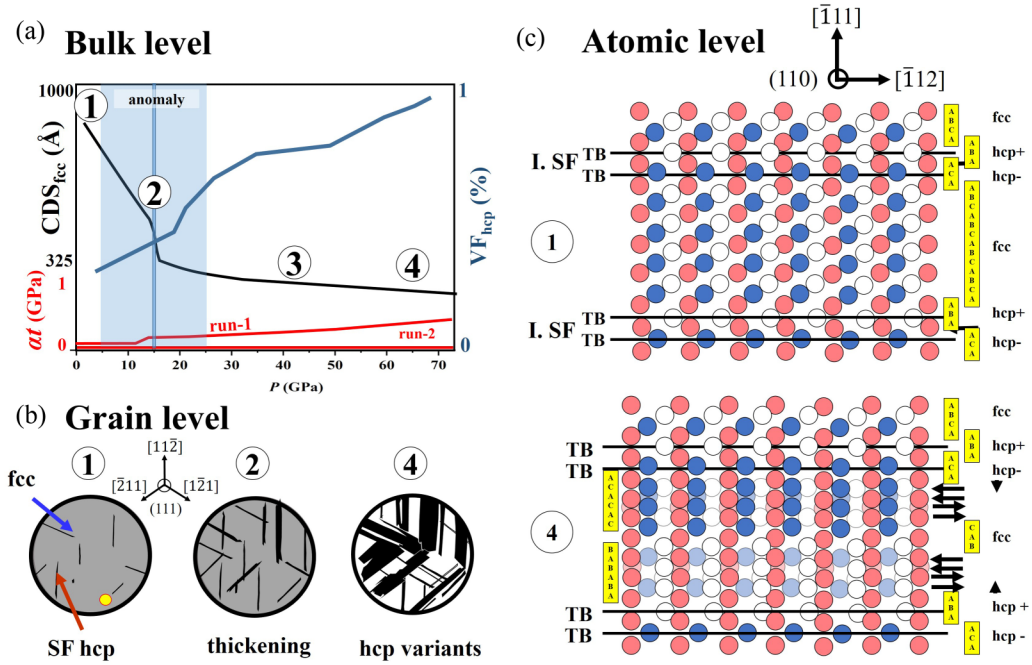

FIG. 9. Evolution of mechanical and microstructural parameters during the martensitic fcc/hcp transition in xenon at (a) the bulk, (b) the grain, and (c) the atomic level. The transition is divided into four transformational stages: (1) nanometric hcp stacking fault (SF) formation from 1.3 GPa onward in xenon, (2) interconnection of SF that induces the compressional anomaly, (3) transformation of remaining fcc domains via shuffling into hcp variant domains of equivalent size, and (4) final microstructure of coexisting hcp variants with inverted stacking sequences. In (a) the pressure dependence of CDS_{fcc}, stress in gold (αt), and VF_{hcp} are summarized. The pressure domain of the compression anomaly is highlighted by a blue-shaded area and the inflexion point of the anomalous compression behavior is delineated by a blue bar. (b) summarizes the progression of the transition at the grain scale for the different stages. The yellow circle represents the size of the x-ray beam. At stage 4, hcp variant domains are shown in black and white, to highlight differences in the hcp stacking sequence of either *ABABA* or ACACA [see (c) for more details]. (c) Stacking-fault formation and thickening mechanisms at the atomic scale that can explain the observations from both XRD and EXAFS. Note that the stacking sequence of close-packed planes along the [−111] is shown in upward direction. Abbreviations are TB: twin boundary, I. SF: inverse stacking fault, hcp+ (*ABA*, stacking sequence) and hcp− (*ACACA*, stacking sequence) .

of preexisting defects (Fig. 2). In the first stage of the transition (stage 1 of Fig. 9), we observe a spontaneous formation of isolated but abundant hcp nanometric stacking faults along the [111] fcc directions at relatively low pressures (∼1.3 and ∼2.7 GPa for xenon and krypton, respectively). Their growth is evidenced by the presence and increasing intensity of diffuse x-ray scattering signal in the vicinity of the fcc Bragg reflections (Figs. 2, 5, S8, S11, and S12). Single-crystal XRD analysis (Figs. S11 and S12) indicates that all possible orientation of hcp domains, with (0001)hcp//(111)fcc (Shoji-Nishiyama orientation relations [1]) are observed; this represents four possible orientations, which we call variants here. This conforms to the general concept of the fcc-hcp martensitic transition developed by Olson and Cohen [65] proposing that the first step in martensitic nucleation is characterized by faulting on planes of closest packing resulting from the spontaneous formation of martensitic embryos. A mechanism responsible for the formation of these nanometric SFs could be the recombination of two Shockley partial dislocations [1], which could generate two twin boundaries in the fcc lattice [Fig. 9(c)]. The formation of a large amount of SFs can also explain the significant decrease of CDS_{fcc} [Fig. 9(a)].

The second stage of the transition is characterized by the interconnection and thickening of hcp SFs, evidenced by the appearance of distinct hcp diffraction peaks at approximately 15 GPa for Kr [32] and 5 GPa in Xe (Figs. 2, S8, and S12). Upon pressure increase, we first observe a rapid and then progressive formation of thin hcp domains which generate more intense XRD peaks (Xe: Figs. 2, 5, S8, and S12; Kr**:** Fig. 4 of Ref. [32]). The formation of a large amount of hcp SFs may explain the strong reduction of the parent-phase grain size [Figs. 6 and 9(a)]. As evidenced from EXAFS and XRD, in the pressure interval of the compression anomaly the hcp form exhibits shorter next-nearest neighbor distances (up to 4% difference for Kr and 1% for Xe) than the parent fcc phase (Xe and Kr, Fig. 7), which may lead to increased local disorder (Fig. 8) and to the buildup of strain in the material at the fcc-hcp structural boundaries. Based on the compiled observations from EXAFS and XRD (Fig. 9), we suggest that the interconnection of dense hcp domains is responsible for the observed compression anomaly in the host fcc phase. This microstructural feature of the transformation is of particular importance as it might be similar to the one responsible for the hardening of metals (i.e., steel hardening). We emphasize that this critical observation can only be made *in situ* and not on quenched materials as the unit-cell volumes and local structures are substantially modified during the quenching process. It is also worth noting that the compression behavior of the gold sample located in the pressure cavity is regular over the entire pressure domain (Figs. S4 and S5, Supplemental Material). This provides additional evidence that the observed compression anomaly in krypton and xenon is intrinsically

due to the fcc-hcp lattice mismatch and intergrowth of hcp variants, but not due to the presence of pressure gradients in the sample chamber.

Based on total energy considerations, under equilibrium conditions, the densities of coexisting fcc and hcp forms should be similar in the two phases. The observed lower density of the hcp SFs could be related to its nanometric and defect nature, as well as to the observed slightly smaller c/a ratio compared to the ideal value that suggests a slightly deformed hcp lattice.

The third stage of the transformation, after the compression anomaly, is more specific to krypton and xenon. This might be because in steel hardening processes, the quenching of the material would be performed at stage 2 of the transformation, when the concentration of strain is maximum. At the third stage, the fcc-hcp lattice difference vanishes and the fcc phase retrieves a regular compression behavior (Figs. 4, 7, and 9(a)]. This is also a clear indication that the hcp-fcc lattice mismatch is at the origin of the strain enhancement and compression anomaly. This third stage is characterized by a stagnation of the CDS_{fcc} and CDS_{hcp} and an increase of the hcp volume fraction VF_{hcp} [Figs. 5, 6, and 9(a)]. Based on these microstructural observations, we propose that this third stage might be characterized by the collective shuffling of remaining fcc domains surrounded by hcp SFs. We assume that the formation of new hcp SFs seeds would result in a more drastic reduction of CDS_{fcc} that is not observed beyond the compressional anomaly (Fig. 6). Our conclusion is consistent with computational studies that reported a favorable formation of hcp SFs seed in larger fcc domains [34]. The simultaneous growth of equivalent-sized hcp variants due to shuffling of atoms minimizes transformational strains [1] and in the present case also reduces nonhydrostatic stresses naturally present in the DAC at high pressure [Figs. S4, S5, and Fig. 9(a)]. It was indeed shown that the formation of coexisting equivalent-sized hcp variants in metals compensates for the strains induced by the martensitic transition due to crystal shape changes [1,53].

Both krypton and xenon preserve the initial strong preferred orientation of the hcp phase (Fig. 2, and Fig. 1 of Ref. [32]) up to the maximum investigated pressure. This suggests that the relative lattice rotations of isolated hcp grains induced by slip systems other than those along the (111) crystallographic planes play a minor role in the transformation. The proposed transformation mechanism would result in a final microstructure of the fully transformed material characterized by a large amount of domain boundaries between hcp variants with fcc-like stacking sequences as illustrated in Fig. 9(c) (stage 4).

V. CONCLUSION

We have examined the fcc to hcp martensitic transformation in solid krypton and xenon using *in situ* XRD and EXAFS. We have evidenced a multistage mechanism in which the transition initially proceeds through the spontaneous nucleation of hcp nanometric domains. This stage is followed by a strain accumulation in the bulk material due to fcc-hcp lattice mismatch and the presence of a large fraction of hcp stacking faults. In this transient domain, an anomaly is evidenced in the equation of state of both materials. In the following stage of the transformation, the lattice mismatch vanishes and a normal compression behavior is retrieved. The microtexture of xenon in the final stage is characterized by the presence of coexisting hcp variants with inverted stacking sequences. The possible formation of equisized hcp variants could explain the low deviatoric stress as seen by the gold pressure marker. The present work reveals the multiple stages of the transformation and disentangles the different effects occurring during the transition. We also provide evidence that the variation of the atomic distances of the parent and martensitic phase during the transformation plays a key role in the building up and accumulation of strain in the materials' structure.

ACKNOWLEDGMENTS

We would like to acknowledge the ESRF for providing beamtime for this work and we are grateful for the help of J. Jacobs during the gas loading of the samples. We also thank F. Perrin and S. Pasternak for their technical assistance during the experiments. Lawrence Livermore National Laboratory is operated by Lawrence Livermore National Security, LLC, for the U.S. Department of Energy, National Nuclear Security Administration under Contract No. DE-AC52-07NA27344.

The original idea was conceived by A.D.R. The experiments were performed by A.D.R., G.G., V.S., G.M., M.K., R.B., and O.M. T.I. provided the nanopolycrystalline diamonds for the x-ray absorption experiments. The data were analysed by A.D.R., A.D., G.G., V.S., F.D.A., and O.M. The manuscript was written by A.D.R. and M.A.B. with contributions from all the coauthors.

The authors declare no competing interests.

[1] Z. Nishiyama, *Martensitic Transformation*, 1st ed. (Academic Press, New York, 1978).

[2] M. Militzer, A synchrotron look at steel, Science **298**, 975 (2002).

[3] D. Fahr, *Enhancement of Ductility in High-Strength Steels* (University of California, Berkeley, 1969).

[4] K. Otsuka and T. Kakeshita, Science and technology of shape-memory alloys. New developments, MRS Bull. **27**, 91 (2002).

[5] B. Ramachandran, P. C. Chang, Y. K. Kuo, C. Chien, and S. K. Wu, Characteristics of martensitic and strain-glass transitions of the Fe-substituted TiNi shape memory alloys probed by transport and thermal measurements, Sci. Rep. **7**, 16336 (2017).

[6] J. I. Perez-Landazabal, V. Recarte, V. Sanchez-Alarcos, J. J. Beato-Lopez, J. A. Rodriguez-Velamazan, J. Sanchez-Marcos, C. Gomez-Polo, and E. Cesari, Giant direct and inverse mag-

netocaloric effect linked to the same forward martensitic transformation, Sci. Rep. **7**, 13328 (2017).

[7] W. G. Burgers, On the process of transition of the cubic-body-centered modification into the hexagonal-close-packed modification of zirconium, Physica **1**, 561 (1934).

[8] A. Dewaele, C. Denoual, S. Anzellini, F. Occelli, M. Mezouar, P. Cordier, S. Merkel, M. Veron, and E. Rausch, Mechanism of the alpha-epsilon phase transformation in iron, Phys. Rev. B **91**, 174105 (2015).

[9] C. S. Yoo, H. Cynn, P. Söderlind, and V. Iota, New B(fcc)-Cobalt to 210 GPa, Phys. Rev. Lett. **84**, 4132 (2000).

[10] R. T. Johnson and R. D. Dragsdorf, The martensitic transformation in cobalt, J. Appl. Phys. **38**, 618 (1967).

[11] M. Jiang, K. Oikawa, and T. Ikeshoji, Molecular-dynamic simulations of martensitic transformation of cobalt, Metall. Mater. Trans. A **36**, 2307 (2005).

[12] T. Komabayashi, Y. Fei, Y. Meng, and V. Prakapenka, *In-situ* X-ray diffraction measurements of the γ-ε transition boundary of iron in an internally-heated diamond anvil cell, Earth. Planet. Sci. Lett. **282**, 252 (2009).

[13] F. X. Zhang, S. Zhao, K. Jin, H. Bei, D. Popov, C. Park, J. C. Neuefeind, W. J. Weber, and Y. Zhang, Pressure-induced fcc to hcp phase transition in Ni-based high entropy solid solution alloys, Appl. Phys. Lett. **110**, 011902 (2017).

[14] G. Fiquet, C. Narayana, C. Bellin, A. Shukla, I. Estève, A. L. Ruoff, G. Garbarino, and M. Mezouar, Structural phase transitions in aluminium above 320 GPa, C. R. Geosci. **351**, 243 (2019).

[15] Y. Akahama, M. Nishimura, K. Kinoshita, H. Kawamura, and Y. Ohishi, Evidence of a fcc-hcp Transition in Aluminum at Multimegabar Pressure, Phys. Rev. Lett. **96**, 045505 (2006).

[16] L. Dubrovinsky, N. Dubrovinskaia, W. A. Crichton, A. S. Mikhaylushkin, S. I. Simak, I. A. Abrikosov, J. S. de Almeida, R. Ahuja, W. Luo, and B. Johansson, Noblest of All Metals Is Structurally Unstable at High Pressure, Phys. Rev. Lett. **98**, 045503 (2007).

[17] J. X. Yang, H. L. Zhao, H. R. Gong, M. Song, and Q. Q. Ren, Proposed mechanism of HCP $\rightarrow$ FCC phase transition in titianium through first principles calculation and experiments, Sci. Rep. **8**, 1992 (2018).

[18] K. Datta, R. Delhez, P. M. Bronsveld, J. Beyer, H. J. M. Geijselaers, and J. Post, A low-temperature study to examine the role of epsilon-martensite during strain-induced transformations in metastable austenitic stainless steels, Acta Mater. **57**, 3321 (2009).

[19] A. K. De, J. G. Speer, D. K. Matlock, D. C. Murdock, M. C. Mataya, and R. J. Comstock, Deformation-induced phase transformation and strain hardening in type 304 austenitic stainless steel, Metall. Mater. Trans. **37a**, 1875 (2006).

[20] A. I. Tyshchenko, W. Theisen, A. Oppenkowski, S. Siebert, O. N. Razumov, A. P. Skoblik, V. A. Sirosh, Y. N. Petrov, and V. G. Gavriljuk, Low-temperature martensitic transformation and deep cryogenic treatment of a tool steel, Mater. Sci. Eng. **527**, 7027 (2010).

[21] U. Dahmen, K. H. Westmacott, P. Pirouz, and R. Chaim, The martensitic-transformation in silicon.2. Crystallographic analysis, Acta Metall. Mater. **38**, 323 (1990).

[22] A. Lai, Z. H. Du, C. L. Gan, and C. A. Schuh, Shape memory and superelastic ceramics at small scales, Science **341**, 1505 (2013).

[23] G. B. Olson and H. Hartman, Martensite and life - displacive transformations as biological processes, J. Phys. **43**, 855 (1982).

[24] Y. F. Shen, Y. D. Wang, X. P. Liu, X. Sun, R. L. Peng, S. Y. Zhang, L. Zuo, and P. K. Liaw, Deformation mechanisms of a 20Mn TWIP steel investigated by in situ neutron diffraction and TEM, Acta Mater. **61**, 6093 (2013).

[25] R. L. Peng, X. P. Liu, Y. D. Wang, S. Y. Zhang, Y. F. Shen, and S. Johansson, *In-situ* neutron diffraction study of the deformation behaviour of two high-manganese austenitic steels, Mater. Sci. Forum **681**, 474 (2011).

[26] J. Liu and D. Kaoumi, Use of *in-situ* TEM to characterize the deformation-induced martensitic transformation in 304 stainless steel at cryogenic temperature, Mater. Charact. **136**, 331 (2018).

[27] X. S. Yang, S. Sun, X. L. Wu, E. Ma, and T. Y. Zhang, Dissecting the mechanism of martensitic transformation via atomic-scale observations, Sci. Rep. **4**, 6141 (2014).

[28] Y. Peng, W. Li, F. Wang, T. Still, A. G. Yodh, and Y. L. Han, Diffusive and martensitic nucleation kinetics in solid-solid transitions of colloidal crystals, Nat. Commun. **8**, 14978 (2017).

[29] E. Kim, M. Nicol, H. Cynn, and C. S. Yoo, Martensitic fcc-to-hcp Transformations in Solid Xenon under Pressure: A First-Principles Study, Phys. Rev. Lett. **96**, 035504 (2006).

[30] H. Cynn, C. S. Yoo, B. Baer, V. Iota-Herbei, A. K. McMahan, M. Nicol, and S. Carlson, Martensitic fcc-to-hcp Transformation Observed in Xenon at High Pressure, Phys. Rev. Lett. **86**, 4552 (2001).

[31] D. Errandonea, B. Schwager, R. Boehler, and M. Ross, Phase behavior of krypton and xenon to 50 GPa, Phys. Rev. B **65**, 214110 (2002).

[32] A. D. Rosa, G. Garbarino, R. Briggs, V. Svitlyk, G. Morard, M. A. Bouhifd, J. Jacobs, T. Irifune, O. Mathon, and S. Pascarelli, Effect of the fcc-hcp martensitic transition on the equation of state of solid krypton up to 140 GPa, Phys. Rev. B **97**, 094115 (2018).

[33] P. Schwerdtfeger, N. Gaston, R. P. Krawczyk, R. Tonner, and G. E. Moyano, Extension of the Lennard-Jones potential: Theoretical investigations into rare-gas clusters and crystal lattices of He, Ne, Ar, and Kr using many-body interaction expansions, Phys. Rev. B **73**, 064112 (2006).

[34] B. Li, G. Qian, A. R. Oganov, S. E. Boulfelfel, and R. Faller, Mechanism of the fcc-to-hcp phase transformation in solid Ar, J. Chem. Phys. **146**, 214502 (2017).

[35] S. Pascarelli, O. Mathon, T. Mairs, I. Kantor, G. Agostini, C. Strohm, S. Pasternak, F. Perrin, G. Berruyer, P. Chappelet, C. Clavel, and M. C. Dominguez, The Time-resolved and Extreme-conditions XAS (TEXAS) facility at the European Synchrotron Radiation Facility: The energy-dispersive X-ray absorption spectroscopy beamline ID24, J. Synchrotron Radiat. **23**, 353 (2016).

[36] O. Mathon, A. Beteva, J. Borrel, D. Bugnazet, S. Gatla, R. Hino, I. Kantor, T. Mairs, M. Munoz, S. Pasternak, F. Perrin, and S. Pascarelli, The time-resolved and extreme conditions XAS (TEXAS) facility at the European Synchrotron Radiation Facility: The general-purpose EXAFS bending-magnet beamline BM23, J. Synchrotron Radiat. **22**, 1548 (2015).

[37] M. Mezouar, J. P. Perrillat, G. Garbarino, W. A. Crichton, S. Bauchau, and H. Witsch, Toward fully automated high pressure beamlines: Recent developments at beamline ID27, ESRF, Acta Crystallogr. A **64**, C610 (2008).

[38] M. Meyer, Twin samples with CrysAlisPro: Experiments, unit cell finding, data reduction and post corrections, Acta Crystallogr. A **68**, S83 (2012).
[39] A. P. Hammersley, FIT2D: A multi-purpose data reduction, analysis and visualization program, J. Appl. Crystallogr. **49**, 646 (2016).
[40] L. Lutterotti, S. Matthies, H. R. Wenk, A. S. Schultz, and J. W. Richardson, Combined texture and structure analysis of deformed limestone from time-of-flight neutron diffraction spectra, J. Appl. Phys. **81**, 594 (1997).
[41] See Supplemental Material at http://link.aps.org/supplemental/10.1103/PhysRevB.105.144103 for raw data and detailed analysis results.
[42] A. Dewaele, A. D. Rosa, and N. Guignot, Argon-neon binary diagram and $ArNe_2$ Laves phase, J. Chem. Phys. **151**, 124708 (2019).
[43] A. Dewaele, M. Torrent, P. Loubeyre, and M. Mezouar, Compression curves of transition metals in the Mbar range: Experiments and projector augmented-wave calculations, Phys. Rev. B **78**, 104102 (2008).
[44] A. D. Rosa, M. A. Bouhifd, G. Morard, R. Briggs, G. Garbarino, T. Irifune, O. Mathon, and S. Pascarelli, Krypton storage capacity of the Earth's lower mantle, Earth. Planet. Sci. Lett. **532**, 116032 (2020).
[45] A. Dewaele, C. M. Pepin, G. Geneste, and G. Garbarino, Reaction between nickel or iron and xenon under high pressure, High Pressure Res. **37**, 137 (2017).
[46] R. Giampaoli, I. Kantor, M. Mezouar, S. Boccato, A. D. Rosa, R. Torchio, G. Garbarino, O. Mathon, and S. Pascarelli, Measurement of temperature in the laser heated diamond anvil cell: Comparison between reflective and refractive optics, High Pressure Res. **38**, 250 (2018).
[47] K. Takemura and A. Dewaele, Isothermal equation of state for gold with a He-pressure medium, Phys. Rev. B **78**, 104119 (2008).
[48] A. D. Rosa, O. Mathon, R. Torchio, J. Jacobs, S. Pasternak, T. Irifune, and S. Pascarelli, Nano-polycrystalline diamond anvils: Key devices for XAS at extreme conditions: Their use, scientific impact, present status and future needs, High Pressure Res. **40**, 65 (2019).
[49] S. Anzellini, A. Dewaele, F. Occelli, P. Loubeyre, and M. Mezouar, Equation of state of rhenium and application for ultra high pressure calibration, J. Appl. Phys. **115**, 043511 (2014).
[50] B. Ravel and M. Newville, ATHENA, ARTEMIS, HEPHAESTUS: Data analysis for X-ray absorption spectroscopy using IFEFFIT, J. Synchrotron Radiat. **12**, 537 (2005).
[51] P. Fornasini, R. Grisenti, T. Irifune, T. Shinmei, O. Mathon, S. Pascarelli, and A. D. Rosa, Bond compressibility and bond Gruneisen parameters of CdTe, J. Phys.: Condens. Matter **30**, 245402 (2018).
[52] A. Filipponi and A. DiCicco, X-ray-absorption spectroscopy and n-body distribution functions in condensed matter. II. Data analysis and applications, Phys. Rev. B **52**, 15135 (1995).
[53] H. Schumann, Hexagonal episolon-phase in iron and iron alloys, Arch. Eisenhuttenwes. **40**, 1027 (1969).
[54] D. Errandonea, R. Boehler, S. Japel, M. Mezouar, and L. R. Benedetti, Structural transformation of compressed solid Ar: An x-ray diffraction study to114 GPa, Phys. Rev. B **73**, 092106 (2006).
[55] A. N. Zisman, I. I. Aleksandrov, and S. M. Stishov, X-ray study of equations of state of solid xenon and cesium iodide at pressures up to 55 GPa, Phys. Rev. B **32**, 484 (1985).
[56] R. J. Angel, M. Alvaro, R. Miletich, and F. Nestola, A simple and generalised P-T-V EoS for continuous phase transitions, implemented in EosFit and applied to quartz, Contrib. Mineral. Petrol. **172**, 29 (2017).
[57] A. Dewaele, P. Loubeyre, P. Dumas, and M. Mezouar, Oxygen impurities reduce the metallization pressure of xenon, Phys. Rev. B **86**, 014103 (2012).
[58] T. Kenichi, Structural study of Zn and Cd to ultrahigh pressures, Phys. Rev. B **56**, 5170 (1997).
[59] A. P. Jephcoat, H.-k. Mao, L. W. Finger, D. E. Cox, R. J. Hemley, and C.-s. Zha, Pressure-Induced Structural Phase-Transitions in Solid Xenon, Phys. Rev. Lett. **59**, 2670 (1987).
[60] R. Jeanloz and R. M. Hazen, Finite-strain analysis of relative compressibilities - Application to the high-pressure Wadsleyite phase as an illustration, Am. Mineral. **76**, 1765 (1991).
[61] B. K. Godwal, S. V. Raju, Z. Geballe, and R. Jeanloz, Electronic phase transitions in cadmium at high pressures, J. Phys. Conf. Ser. **377**, 012033 (2012).
[62] N. C. Popa and D. Balzar, An analytical approximation for a size-broadened profile given by the lognormal and gamma distributions, J. Appl. Crystallogr. **35**, 338 (2002).
[63] A. DiCicco, A. Filipponi, J. P. Itie, and A. Polian, High-pressure EXAFS measurements of solid and liquid Kr, Phys. Rev. B **54**, 9086 (1996).
[64] R. A. Aziz and M. J. Slaman, The argon and krypton interatomic potentials revisited, Mol. Phys. **58**, 679 (1986).
[65] G. B. Olson and M. Cohen, A general mechanism of martensitic nucleation: Part I. General concepts and the FCC → HCP transformation, Metall. Trans. A **7**, 1897 (1976).